Batteries & Supercaps

Research Article
doi.org/10.1002/batt.202500378

Chemistry Europe
European Chemical Societies Publishing

www.batteries-supercaps.org

In-Depth Analysis of the Origin of Enhanced Ionic Conductivity of Halide-Based Solid-State Electrolyte by Anion Site Substitution

Priya Ganesan,* Ramon Zimmermanns, Jianneng Liang, Yang Hu, Gabriel J. Cuello, Inés Puente Orench, Sebastian Baumgart, Mohsen Sotoudeh, Axel Groß, Thomas Diemant, Alberto Varzi,* and Maximilian Fichtner

Halide-based solid-state electrolytes (HSEs) offer higher anodic stability than sulfide solid electrolytes with Li_2ZrCl_6 (LZC) standing out due to its low cost and elemental abundance. However, its limited ionic conductivity has inhibited wider application up to now. In this context, S-doped Li_2ZrCl_6 (LZCS) electrolytes that reach a conductivity of up to 0.64 mS cm^{-1} (3 times higher than pristine LZC, 0.21 mS cm^{-1}) with good electrochemical stability have been synthesized and studied. X-ray and neutron diffraction reveal the coexistence of monoclinic and trigonal phases in LZCS, which is the probable reason for enhanced ionic conductivity. The monoclinic phase with antisite disorder leads to 2D diffusion pathway, which is confirmed by density functional theory simulations. Stripping/plating results show that $Li_2ZrCl_{5.6}S_{0.2}$ exhibits the smallest polarization over 600 h at 0.1 mA cm^{-2}. Full cell tests with $LiNi_{0.6}Mn_{0.2}Co_{0.2}O_2$ (NMC622) positive electrode further demonstrate a better capacity retention of 96.3% for $Li_2ZrCl_{5.6}S_{0.2}$ (LZCS02) in comparison to that of Li_2ZrCl_6 (68.5%).Focused ion beam (FIB) line scans show less nickel and oxygen diffusion at the LZCS02/NMC622 interface. In this study, an in-depth analysis of the structure and ionic conductivity relationship in S-doped Li_2ZrCl_6 HSEs is provided, opening a new approach for designing highly performing HSEs.

1. Introduction

The growing demand for more energy-efficient and safer energy storage systems has accelerated the transition from conventional Li-ion batteries (LIBs) to all-solid-state batteries (ASSBs), which has potential advantages, such as enhanced safety, wider operating temperature range, and higher energy density.[1,2] In this context, ASSBs with different anion chemistries have been explored, including oxides,[3] sulfides,[4] borohydrides,[5] and halides.[6] Each of these has its own advantages and disadvantages in terms of the ease of synthesis, ionic conduction, electrochemical stability, and atmospheric stability. In this regard, halide solid electrolytes (HSEs) have gained significant interest due to their relatively high room-temperature ionic conductivity (10^{-3}–10^{-4} S cm^{-1}) and compatibility with high-voltage cathodes (>4 V).[7]

In general, the crystallographic structure of HSEs is influenced by the packing arrangement of the Li-*M*-X (M = In, Y, Er, Sc, Zr, etc., X = Cl, Br, I) system based on the ratio of cation-to-anion radius and the size of metal ion (M).[8,9] Especially for ternary halide HSEs, two anion sublattice structures are possible with either hexagonal close packing (hcp) or cubic close packing (ccp) of the anions.[10] The arrangement of the anion sublattices in either hcp or ccp gives rise to trigonal, orthorhombic, or monoclinic structures, with each leading to different Li-ion diffusion pathways.[11,12] For example, in a ccp lattice, a network of octahedral and tetrahedral sites creates 3D diffusion pathway for the Li^+ ions, while the hcp lattice promotes 1D diffusion channels constituted by face-sharing octahedral sites. Then, different diffusion pathways invariably affect the migration barrier and the Li-ion conductivity of the solid electrolyte.[13] Both Li_3YCl_6 and Li_2ZrCl_6 crystallize in hcp anion lattice and exhibit 1D diffusion channels with an ionic conductivity of <1 mS cm^{-1}.[14,15] In contrast, Li_3InCl_6 crystallizes in monoclinic (ccp) lattice with 3D diffusion pathways, resulting in an higher ionic conductivity of 1.06 mS cm^{-1}.[16] The difference in ionic conductivity supports the idea that a ccp anion lattice generally leads to an increased ionic conductivity in HSEs. The general trend of ionic conductivities of HSEs is σ (monoclinic) > σ (orthorhombic) > σ (trigonal).

P. Ganesan, R. Zimmermanns, J. Liang, Y. Hu, M. Sotoudeh, A. Groß,
T. Diemant, A. Varzi, M. Fichtner
Helmholtz Institute Ulm (HIU) Electrochemical Energy Storage
Helmholtzstrasse 11, 89081 Ulm, Germany
E-mail: priya.ganesan@kit.edu
alberto.varzi@kit.edu

P. Ganesan, R. Zimmermanns, J. Liang, Y. Hu, T. Diemant, A. Varzi,
M. Fichtner
Karlsruhe Institute of Technology (KIT)
P.O. Box 3640, 76021 Karlsruhe, Germany

G. J. Cuello, I. Puente Orench
Institute Laue-Langevin
Grenoble 38042, France

S. Baumgart, M. Sotoudeh, A. Groß
Institute of Theoretical Chemistry
Ulm University
Oberberghof 7, 89081 Ulm, Germany

Supporting information for this article is available on the WWW under https://doi.org/10.1002/batt.202500378

The observed trend signifies how the crystal structure plays a critical role in fine tuning the Li-ion conduction mechanism of an HSE.

The presence of stacking faults and mixed phases in the system also influences the ionic conductivity and activation energy of HSEs.[17] In the Li-*M*-X system (M = metal), M has three Wyckoff sites with 1a and 2 d sites occupied by M1 and M2. M3 present in the M2 equivalent site in the (001) plane enables the formation of M2–M3 site disorder that, in turn, enhances the ionic conductivity by reducing the lithium migration energy barrier along the *c*-axis.[18] This disorder, however, is only present in mechanochemically synthesized compounds and not in those obtained by high-temperature sintering. Heat treatments have shown to reduce the M2–M3 site disorder and, hence, lead to a decrease in room-temperature ionic conductivity.[19] Aliovalent or isovalent substitutions could induce phase transitions from trigonal to orthorhombic or monoclinic structures, depending on the amount of substitution for a respective system. For instance, in Li_2ZrCl_6, In and Er dopings on the Zr^{4+} site have shown improved ionic conductivities ($1.08\ mS\ cm^{-1}$ for $Li_2Zr_{1-x}In_xCl_6$ and $1.13\ mS\ cm^{-1}$ for $Li_{3-x}Er_{1-x}Zr_xCl_6$) owing to the transition from trigonal to orthorhombic phases.[20,21] Moreover, site disorder can alter the energy landscape for the Li-ion diffusion.[22]

Extensive studies have been carried out to understand how the structure of halide-based electrolytes affects the Li-ion conductivity.[23–25] Many studies currently focus on mixed anion doping to improve the ionic conductivity at room temperature.[26,27] For example, by bromine doping, the $Li_3YCl_3Br_3$ could achieve a high ionic conductivity of $7.2\ mS\ cm^{-1}$ owing to the phase transition from hcp to ccp and to the formation of large polyhedral faces.[28] However, the high-temperature synthesis, low abundance of Y, and lower oxidative stability of Br are non-negligible disadvantages. In this regard, the earth abundant zirconium (Zr) would make Li_2ZrCl_6 a much more economically viable solid electrolyte. In terms of anion doping, fluorine has shown to improve the interface stability in Li_2ZrCl_6.[29] However, a decrease in ionic conductivity is evident due to the presence of more electronegative fluorine ions. While oxygen and sulfur dopings have been studied for this class of materials, a detailed structure–property correlation and the beneficial effects of dual phase systems have not been fully explored yet.[30,31] Hence, a deeper understanding of the anion sublattice could facilitate material design, aiding in the development of electrolytes with high ionic conductivity, economic viability, elemental abundance, and better stability such as Li_2ZrCl_6.

In this study, we investigate the influence of the inductive effect by substituting a divalent ion (sulfur) into the lattice of Li_2ZrCl_6. A series of sulfur-doped $Li_2ZrCl_{6\text{-}2x}S_x$ ($0 \leq x \leq 0.5$) compounds are synthesized and systematically characterized using X-ray diffraction (XRD), high-resolution neutron powder diffraction (NPD), neutron pair distribution function (NPDF) analysis, and computational studies. In addition, electrochemical studies and focused ion beam (FIB) milling line scans were performed on cycled samples. For clarity, the compounds are referred to by the following abbreviations: LZC ($x = 0$), LZCS01 ($x = 0.1$), LZCS02 ($x = 0.2$), LZCS03 ($x = 0.3$), LZCS04 ($x = 0.4$), and LZCS05 ($x = 0.5$).

2. Results and Discussion

2.1. Physicochemical Characterization

$Li_2ZrCl_{6\text{-}2x}S_x$ ($0 \leq x \leq 0.5$) was synthesized by a mechanochemical method and characterized systematically. The X-ray diffractograms (Figure S1, Supporting Information, $\lambda = 0.7093$ Å) reveal that LZC crystallizes in the trigonal $P\bar{3}m1$(#164) space group. In the trigonal structure, chloride ions are arranged in a hcp lattice, with Zr and Li occupying the octahedral voids (forming edge-sharing $ZrCl_6$ and $LiCl_6$ octahedra along the *c*-axis). As the S doping increases, the (002) reflection at ≈13.7° gradually shifts to lower 2θ values, suggesting that S substitution at the Cl site leads to an expansion of the unit cell. This shift is attributed to the ionic radius difference between S^{2-} (170 pm) and Cl^{-} (167 pm).

Due to the limited ability to probe lighter elements, such as lithium, and to resolve structural details in materials with low crystallinity, XRD proved insufficient to investigate the detailed structural changes. To address these limitations, NPD and NPDF analyses were employed. These techniques offer distinct advantages in determining the position of light elements (lithium) and enable the characterization of both long-range and short-range structural features. Since stacking faults are difficult to resolve using neutron diffraction owing to their small-scale nature and honey comb structures do not significantly influence the anion substructure, an ordered monoclinic model was chosen for the refinement. This model provided an excellent fit to the experimental data, consistent with previous studies in similar systems. To reduce the number of refined parameters and increase the reliability of the refinement, the trigonal structure was fixed with the refined values from Li_2ZrCl_6. Only the unit cell parameters were further refined. As the substitution of S seemingly causes the reordering of the cations to form the monoclinic polymorph, all S atoms were assumed to be present in the monoclinic phase. The refinements and their results are discussed below.

A single-phase refinement was performed on undoped LZC in the $P\bar{3}m1$(#164) space group with two Li sites (Li (1) and Li (2)). In contrast, to fit $Li_2ZrCl_{6\text{-}2x}S_x$, both trigonal ($P\bar{3}m1$) and monoclinic (C2/m) structures were essential for the refinement. **Figure 1**a–d shows the Rietveld refinements of LZC and one of the representative LZCS05 along with the VESTA images depicting the hcp and ccp anion arrangements of LZC/LZCS. The refinement results of the other $Li_2ZrCl_{6\text{-}2x}S_x$ ($x = 0.1$, 0.3, 0.4 & 0.5) compounds are depicted in Figure S2, Supporting Information along with a description of their refinement procedure. The table with the Wyckoff sites and the positions are provided in the supplementary information (Table S1–S6, Supporting Information).

The neutron diffractograms ($\lambda = 1.594$ Å) depicted in **Figure 2**a show similar observations to XRD diffractograms (Figure S1, Supporting Information, $\lambda = 0.7093$ Å). The formation of a new peak at 22.5° was evident with a change in intensity in the preceding peaks, which can be assigned to the monoclinic structure (C2/*m*).

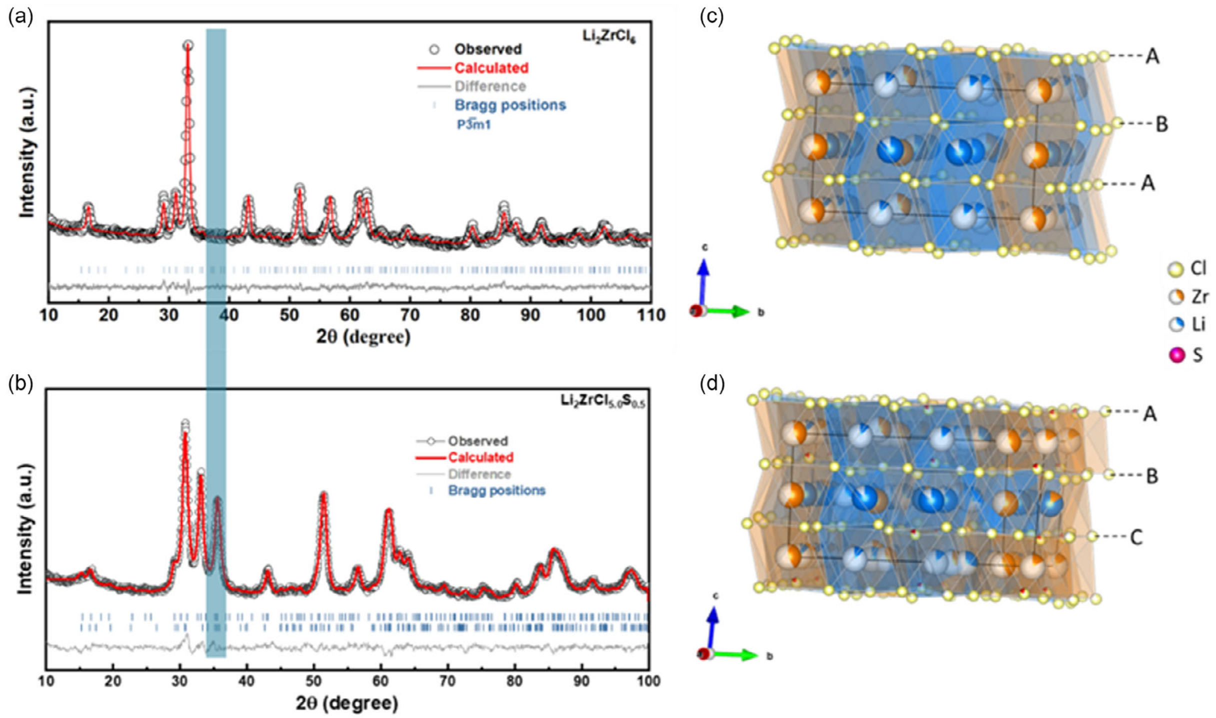

Figure 1. Neutron diffraction patterns ($\lambda = 1.594$ Å) and the corresponding refinement of a) Li_2ZrCl_6 and b) $Li_2ZrCl_{5.0}S_{0.5}$. c,d) Visual representations of the trigonal and monoclinic phases, respectively. In the trigonal phase c), the hcp anion arrangement with ABABAB along the *c*-direction is depicted. The Zr atom is present at Zr1 (1a), Zr3 (1b), Zr2, and Zr4 (2 d) sites with partial occupancy (Table S1, Supporting Information). For the monoclinic phase d), the ccp anion arrangement along the *c*-direction illustrates the ABCABC arrangement. The Zr atom occupies the Zr1 (2a) and Zr2 (4 g) sites. The 2d site is shared with Li (Table S2, Supporting Information) (color codes: orange, blue, yellow, and pink represent zirconia, lithium, chlorine, and sulfur, respectively, while white represents the vacancies).

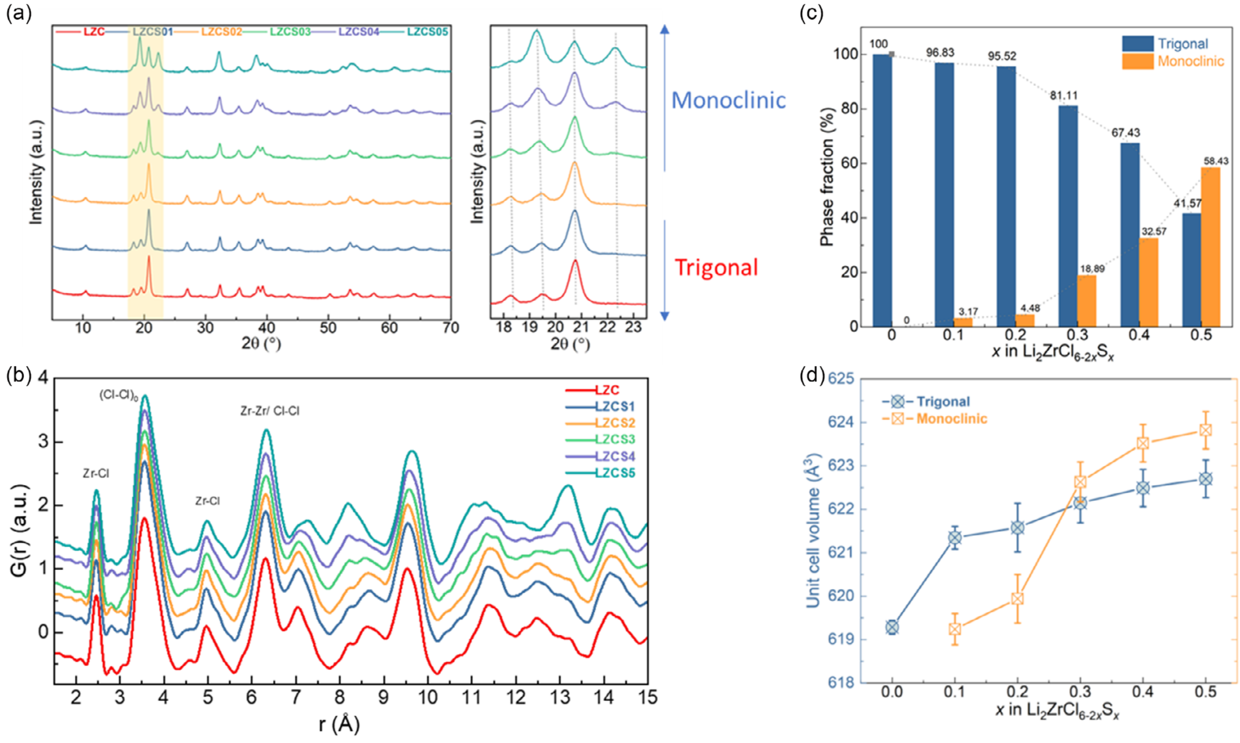

Figure 2. a) Neutron diffraction patterns of $Li_2ZrCl_{6-2x}S_x$ ($0 \leq x \leq 0.5$) compounds with the magnified view of the 2θ range 17°–24°. b) NPDFs G(r) of $Li_2ZrCl_{6-2x}S_x$ ($0 \leq x \leq 0.5$). c) Development of phase fractions (%) with increasing sulfur concentration with error <1%. d) Change of unit cell volume of $Li_2ZrCl_{6-2x}S_x$ ($0 \leq x \leq 0.5$) for both trigonal (blue) and monoclinic phases (orange).

The phase fractions and the unit cell volume changes are depicted in Figure 2c,d. With increasing S concentration, the trigonal phase fraction decreases from 100 ± 1.1 % for undoped to 41.57 ± 0.7 % for $x = 0.5$. A simultaneous increase in the monoclinic phase is evident with the phase fraction being 58.43 ± 1.8 % for $x = 0.5$. The unit cell volume of both phases increases with increasing S concentration. The trigonal phase shows a growth of the unit cell volume from 619.28 ± 0.16 Å^3 for LZC to 622.70 ± 0.43 Å^3 for LZCS05 and monoclinic from 419.24 ± 0.8 Å^3 for LZCS01 to 423.82 ± 0.43 Å^3 for LZCS05. This clearly demonstrates the lattice expansion of the unit cell, which further confirms the presence of sulfur in the lattice.

2.1.1. Local Structure Exploration of LZCS

The local environment of LZCS was investigated using the NPDF analysis; the corresponding G(r) profiles are presented in Figure 2b. The pair distribution function (PDF) fits and the refinement table for $Li_2ZrCl_{6-2x}S_x$ ($0 \leq x \leq 0.5$) are provided in the supplementary information (Figure S3 and Table S7–S12, Supporting Information). A comparison of the results across all LZCS compositions reveals a similar local environment, indicating an identical crystal framework, consistent with the findings from NPD. The primary distinction between the two phases lies in the ordering of Li and Zr, as discussed previously. In both phases, the metal cations are octahedrally coordinated, and the anion sublattice remains barely unaffected by the substitution.

The first two peaks in the PDFs correspond to the Li—Cl bond length of 2.45 Å and a Cl—Cl bond length of 3.56 Å. Notably, the PDFs for all compositions feature a single Cl—Cl peak around 3.56 Å. A shoulder at higher r values suggests the presence of two distinct octahedral species, most likely —$ZrCl_6$ and —$LiCl_6$; however, due to the small differences in Zr—Cl and Li—Cl bond lengths, these peaks overlap significantly. The Li/Zr site disorder is most likely facilitated by the similarities in the ionic radii and the coordination environment of the octahedral sites, which promotes exchange between the metal sites.

Beyond 4 Å, the second coordination shell, corresponding to Zr—Cl, Zr—Zr, and Cl—Cl interactions, becomes visible, though the peaks overlap such that a definitive assignment is challenging. As a result, no significant changes are observed in the PDFs up to ≈6 Å. The absence of additional peaks upon sulfur substitution suggests that S occupies the Cl positions within the lattice. A notable increase in the monoclinic phase fraction is observed in the mid-r region (>7 Å) for the compositions with $x \geq 0.3$.

The evolution of lattice parameters (**Figure 3**a,b) and polyhedral volumes (Figure 3c,d) as a function of S concentration is

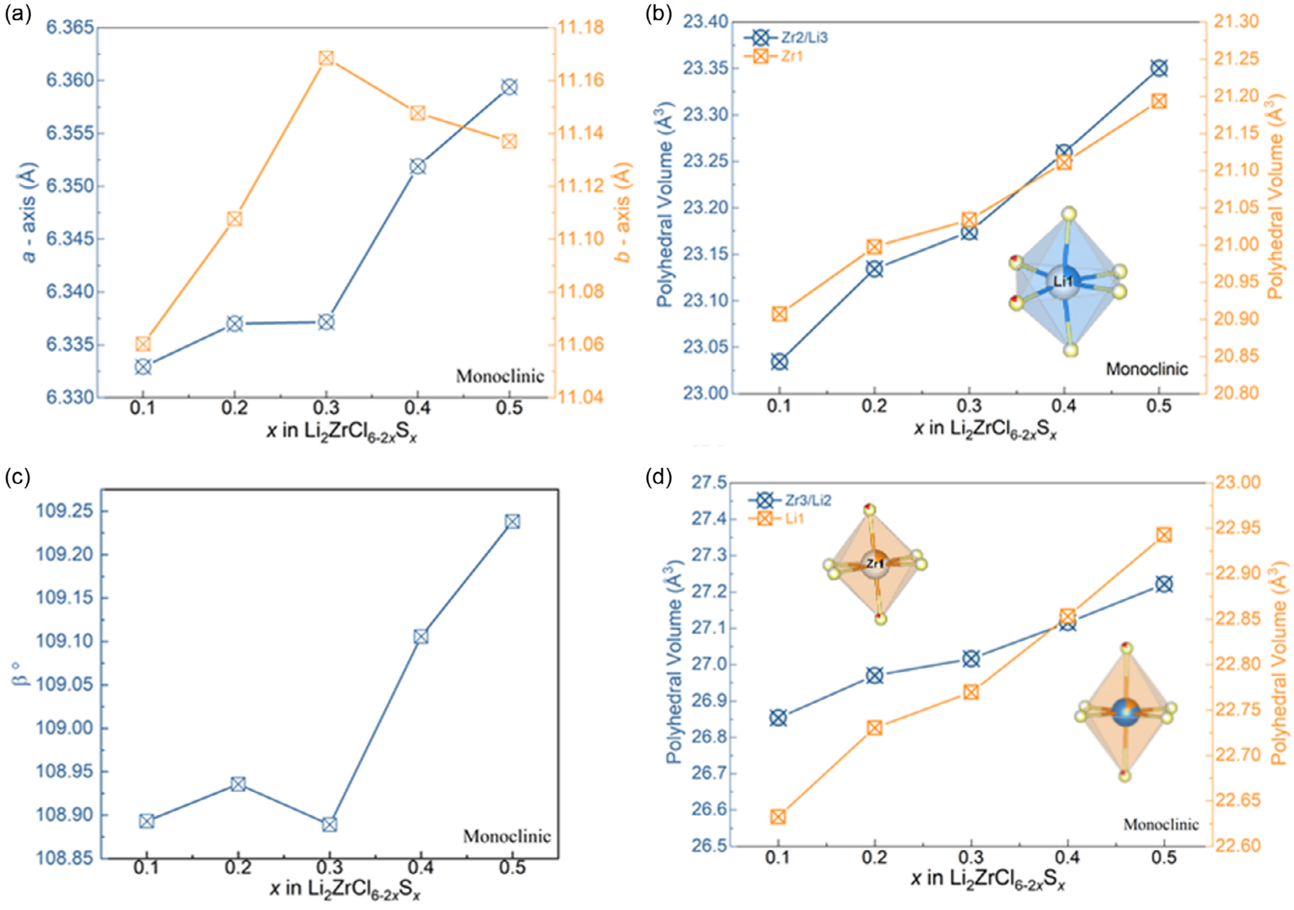

Figure 3. Unit cell parameters in the monoclinic phase of the $Li_2ZrCl_{6-2x}S_x$ ($0 \leq x \leq 0.5$) compounds. a) a and b axis parameters, b) change in β° parameter. c,d) Development of zirconium and lithium polyhedral volumes in the monoclinic phase (the colors yellow, blue, orange, pink and white in the figure represent chlorine, lithium, zirconium, sulfur, and vacancies, respectively).

depicted in Figure 3. For the monoclinic phase, a parameter increases gradually with increasing S doping, consistent with the larger ionic radius of S^{2-} compared to that of Cl^{-}. The b parameter exhibits a nonmonotonic behavior: it increases from $x = 0.1$ to 0.3 followed by a decrease for $x = 0.4$ and 0.5. This nonlinear trend is correlated with changes in the unit cell angle β, which increases concurrently with a decrease in the b parameter (Figure 3b). A similar trend has been observed before for In-doped Li_2ZrCl_6 by Kwak et al. and attributed the nonlinear variations in lattice parameters and the resulting crystal structure distortion to the mixed ionic–covalent bonding character.[32] A similar explanation may apply in the present case, given the lower electronegativity of S compared to that of Cl. This asymmetric expansion accounts for the increase in the unit cell volume shown in Figure 2d. Additionally, the variation in the M–Cl bond lengths within the MCl_6 octahedra (Figure S4a,b, Supporting Information) supports the anisotropic changes.

The volumes of the Li and Zr polyhedra in the monoclinic phase increase steadily with increasing S concentration (Figure 3c,d), further confirming the incorporation of S into the lattice. The corresponding structural changes in the trigonal phase are illustrated in Figure S4, Supporting Information. For the trigonal phase (Figure S4c, Supporting Information), both the a and c parameters expand with increasing S concentration, consistent with the observed increase in unit cell volume. In contrast, the Zr polyhedral volumes (Figure S4d, Supporting Information) remain relatively unchanged from $x = 0.1$ to 0.5, with only a subtle variation between $x = 0$ and 0.1.

Next, the morphology and chemical composition of the LZCS materials were examined. Scanning electron microscopy (SEM) images, along with energy-dispersive X-ray (EDX) mapping results for Zr, Cl, and S, are presented in Figure S5, Supporting Information. The SEM analysis reveals an array of irregularly shaped agglomerated particles across all S-doped materials. EDX mapping further confirms a homogeneous distribution of Zr, Cl, and S within the samples. The chemical state of S was further analyzed by XPS measurements. The detailed spectra in the S 2p range (Figure S6a, Supporting Information) show for all S concentrations a single peak doublet (S $2p_{3/2}$ peak at 161.4 eV), which can be assigned to the sulfide anions in the LZCS compounds. The results demonstrate the absence of other S species (disulfide, elemental, etc.). In addition, Figure S6b, Supporting Information shows the results of S *K*-edge high-energy resolution fluorescence detection–X-ray absorption near-edge structure (HERFD–XANES) measurements of the LZCS compounds, in comparison with $V_4^{3+}V^{4+}(S^{2-})_8$, $Mo^{4+}(S^{2-})_2$, and $Ti^{4+}\ (S^{2-})_2$ standards. As a direct probe of the S 3*p* valence states due to dipole-allowed 1*s*-3*p* transitions, S *K*-edge XAS has been known to show a strong correlation between oxidation state and the energy position, as well as rich spectral structures that are related to the chemical structure and site symmetry and are influenced by the strong *p*–*d* mixing between S and transition metals. In this work, all LZCS samples demonstrated features in the energy range of sulfide (S^{2-}) and disulfide (S_2^{2-}) and no sign of peaks indicating the existence of sulfate (S^{6+}) or sulfite (S^{4+}). At low S concentration, the two features in the spectra might be associated with the hybridization of S 3*p* empty antibonding states with the Zr empty 4 *d* states of octahedrally coordinated Zr with, *e.g.*, t_{2g} symmetry, similar to the case of TiS_2, given the fact that all Zr were considered to be octahedrally coordinated.[33] With increasing S concentration, a new feature arises at about 2471.8 eV, which might suggest a further splitting of Zr 3 *d* states with stronger distortion of Zr octahedra introduced by the S substitution for Cl.

2.2. Impact of the Sulfur Doping on Conduction

The next step involves the determination of ionic conductivity and activation energy (Ea) through electrochemical impedance spectroscopy (EIS). The representative Nyquist plots at 30 °C and the corresponding Arrhenius plots are shown in **Figure 4**a,b. Ionic conductivity was then calculated from the resistance using equation (1) in the supplementary information (**S7**), and the activation energy was extracted from the Arrhenius plot of ionic conductivities measured at varying temperatures as given in equation (2) in S7.

Figure 4c,d illustrates the trends in ionic conductivity and activation energy for LZC and LZCS SSEs. The ionic conductivity at 30 °C ranged from 0.21 to 0.64 mS cm^{-1}, with activation energies between 0.22 and 0.24 eV. The highest ionic conductivity, 0.64 mS cm^{-1}, was observed for LZCS03 attributed to the dual phase structure, as discussed in section 2.1. The measured ionic conductivities for compositions with $x = 0$, 0.1, 0.2, 0.3, 0.4, and 0.5 were 0.21, 0.59, 0.63, 0.64, 0.56, and 0.47 mS cm^{-1}, respectively. The trend of initially increasing ionic conductivity, followed by a decrease after reaching a maximum, can be explained by the dual phase behavior and the corresponding phase fractions (Figure 2c). The observed decline in conductivity for $X > 0.3$ could indicate the formation of isolated Li_2S or LiCl phases. The activation energies were found to be 0.23, 0.22, 0.22, 0.23, and 0.23 eV for $x = 0.1$, 0.2, 0.3, 0.4, and 0.5, respectively, with the lowest value of 0.22 eV for LZCS02. This trend aligns well with the structural evolution upon sulfur substitution, where the mixture of trigonal and monoclinic phases enhances ionic conductivity, although a decrease is observed at higher sulfur concentrations.

Combining the results from neutron diffraction, PDF analysis, and EIS, the biphasic structure has shown to enhance ionic conductivity. The possible reasons for the enhancement are discussed in the following section. The maximum ionic conductivity is achieved for LZCS03 with a phase composition of 81.1 ± 0.8 % trigonal and 18.9 ± 1.3 % monoclinic, corresponding approximately to a 4:1 phase ratio. Therefore, a controlled balance between the trigonal and monoclinic phases is advantageous, as their coexistence contributes to improved structural and electrochemical properties.

Additionally, the electronic conductivity of these HSEs is in the range of 10^{-10} S cm^{-1} (Figure S8, Supporting Information), which is ≈6 orders of magnitude lower than the ionic conductivity, confirming the electronically insulating nature of these compounds. Our findings underscore that understanding the interplay between crystal structure and ion migration pathways is critical for enhancing the ionic conductivity of HSEs. Furthermore, Table S13, Supporting Information, provides a

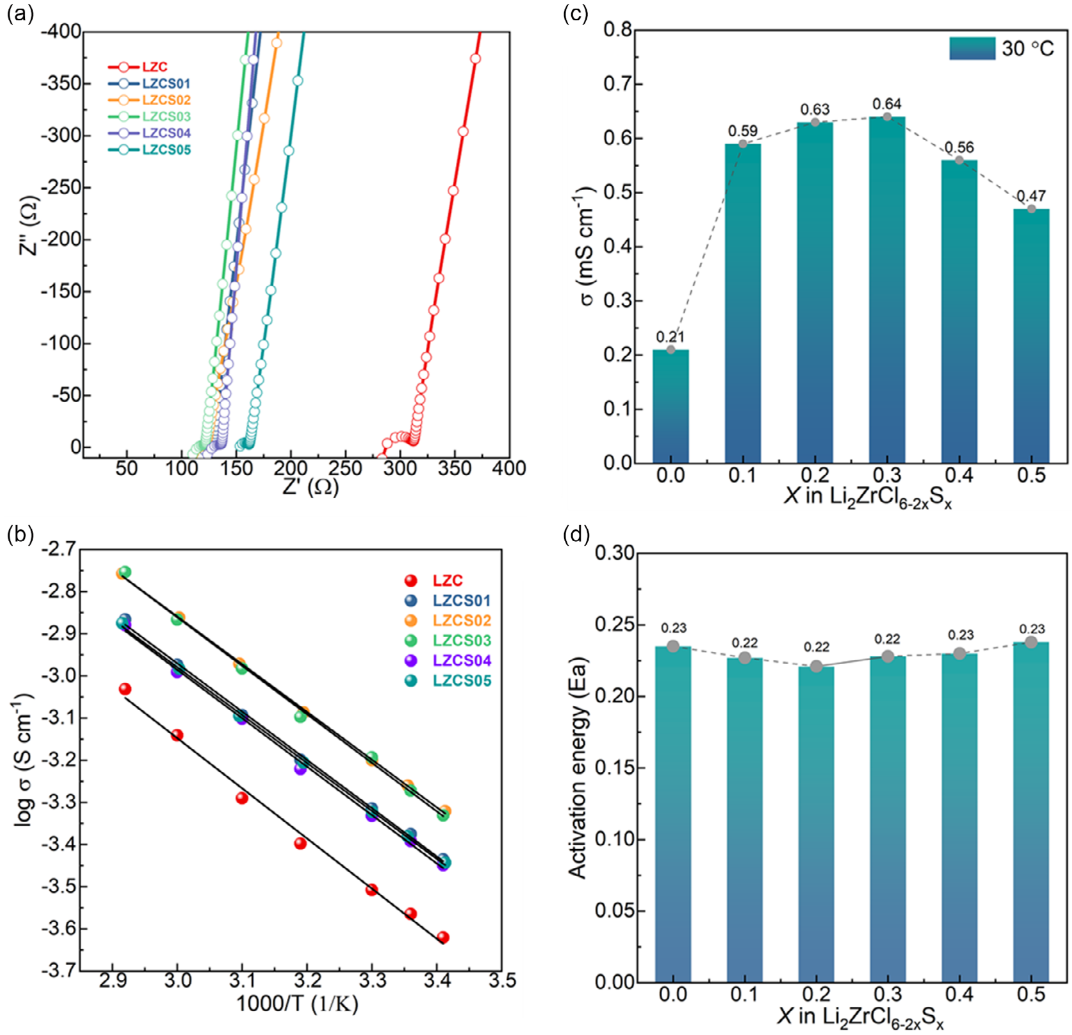

Figure 4. a) Nyquist plots of $Li_2ZrCl_{6-2x}S_x$ ($0 \leq x \leq 0.5$) at 30 °C. b) Arrhenius plots with log σ versus 1000/T from 343 K to 293 K. Bar diagram of the c) ionic conductivity at 30 °C and d) activation energy as a function of sulfur content.

comparative summary on the ionic conductivity, activation energy, and battery performance of different Zr-based electrolytes along with the present work.

2.3. DFT Simulations

DFT simulations were employed to investigate the structural and energetic properties of the system upon sulfur substitution. The doping process involves the removal of two chlorine atoms, followed by the introduction of a single sulfur atom. Two distinct scenarios were considered to analyze the effects of spatial configuration: the removal of chlorine atoms either in proximity or farther apart within the lattice. The computational results indicate that the configuration involving the removal of closely situated chlorine atoms is energetically favored, exhibiting a stability increase of ≈0.16 eV compared to the configuration with far-apart chlorine vacancies. This enhanced stability is attributed to the localized electronic and structural interactions facilitated by the sulfur substitution in the closely positioned configuration. The stable configuration, associated with the removal of closely spaced chlorine atoms, is shown in Figure S9, Supporting Information.

For the $P\bar{3}m1$ space group, two different migration pathways are observed: out-of-plane migration, where lithium transitions directly between octahedral sites through an intervening face-sharing triangle that acts as a transition state as it migrates along the z-direction (**Figure 5**a), and in-plane migration, where lithium moves from an octahedral site to an adjacent tetrahedral site before reaching a nearby octahedral site (Figure 5b). In the $C2/m$ space group, the lithium-ion migration follows a single possible path, moving from the Li plane to the Zr plane along the z-direction (Figure 5c). In this process, the Li-ion transitions from one octahedral site to an adjacent octahedral site via an intervening tetrahedral site.

To calculate the activation energy for these migration processes with good accuracy, the nudged elastic band (NEB) approach was employed, yielding trends consistent with BVSE predictions of ion migration pathways based on electrostatic interactions and bond valence principles. The corresponding BVSE profiles are depicted in **Figure 6**a–c. The more open

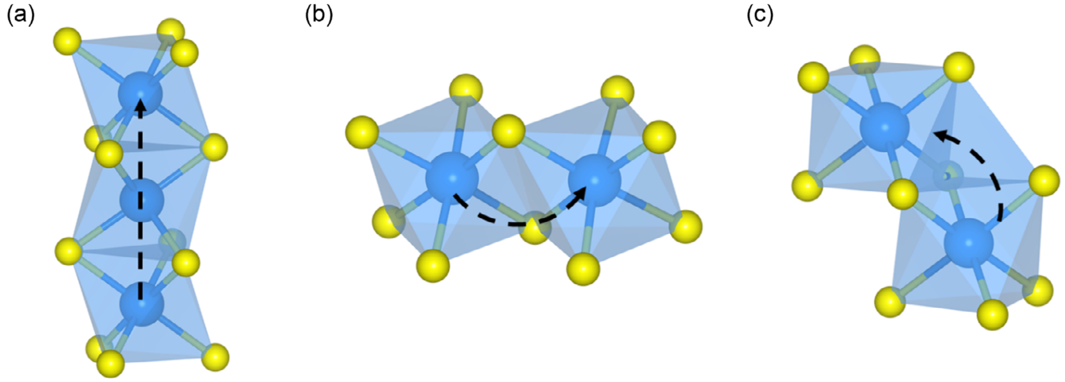

Figure 5. Diffusion mechanisms through different pathways: a) P$\overline{3}$*m*1—direct octahedral to octahedral transition without involving a tetrahedral site, b) P$\overline{3}$*m*1—in-plane diffusion from one octahedral site to another via an intermediate tetrahedral site, and c) C2/*m*—out-of-plane octahedral to octahedral diffusion through a tetrahedral site. Lithium atoms are blue, chlorine atoms are yellow, and polyhedrons are light/transparent blue. The diffusion paths are shown as dashed lines.

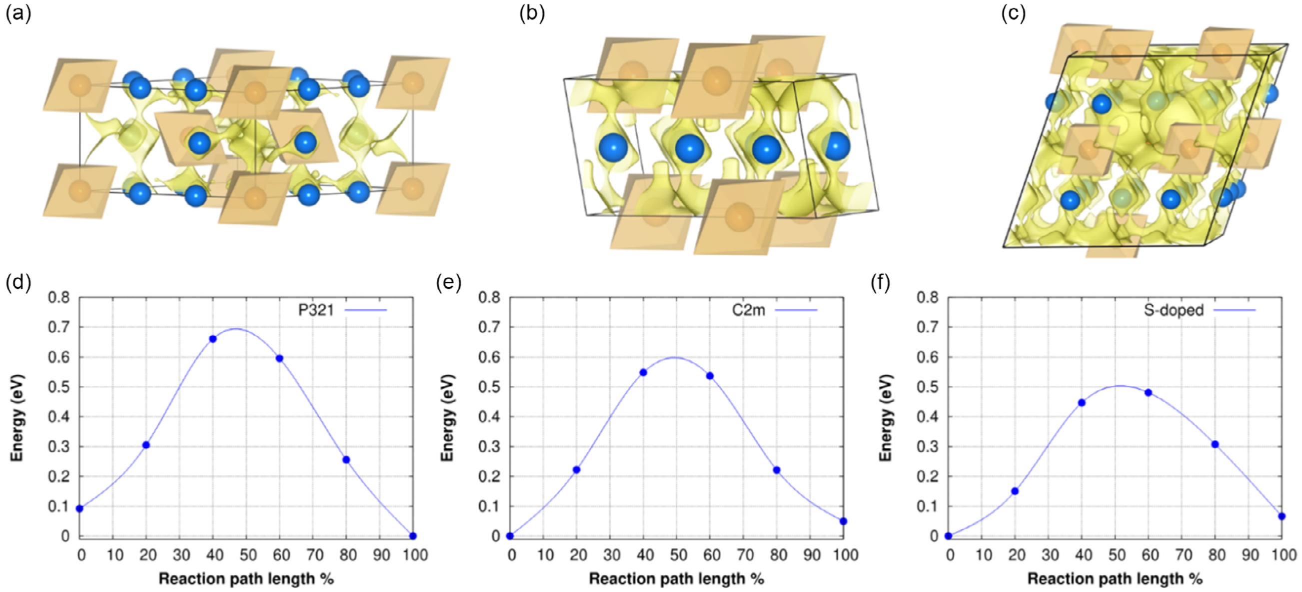

Figure 6. a–c) Simulated BVSE profiles comparing the pristine compounds with the S-doped compound (corresponding stable configuration is shown in Figure S9, Supporting Information). Blue spheres represent lithium atoms, while orange octahedrons depict Zr atoms coordinated by chlorine in an octahedral fashion. The yellow surfaces illustrate pathways for lithium-ion migration. The isovalue is set to 0.35 e/Å^3. d–f) Energy barriers (in eV) for Li$^+$ ion migration plotted against the reaction path coordinate (d–f), obtained via periodic DFT calculations in combination with NEB method. The migration occurs between two octahedral sites across the sharing triangular face. NEB results illustrate the energy profiles for the pristine materials (d and e) and the S-doped material (f).

and continuous migration pathway (highlighted by the yellow isosurfaces) is estimated in the S-doped system compared to the pristine structure. This is reflected in the activation energies calculated by NEB, which were found to be ≈0.7 eV for the trigonal phase (Figure 6d) and 0.6 eV for the monoclinic phase (Figure 6e). Notably, the results show that the S-doped system has been shown to enhance the connectivity between the channels, facilitating the formation of a 2D ion migration network. This modification reduces the activation energy further to 0.5 eV (Figure 6f) and alters the migration dynamics.

This trend mirrors the ionic conductivity patterns discussed in section 2.2 and is likely attributed to the creation of 2D diffusion channels facilitated by sulfur doping and the introduction of vacancies. Vacancy formation is known to influence the migration barriers, potentially lowering the activation energy for ion transport.[34,35] However, due to structural complexity, a direct correlation between the vacancies and the diffusion pathways could not be conclusively established through refinement or simulations. Nevertheless, the sulfur-doped LZCS system demonstrates enhanced ionic conductivity with reduced activation energy. This improvement can be attributed to two key factors: 1) the formation of a biphasic mixture (trigonal and monoclinic phases) and 2) the presence of 2D diffusion pathways facilitating ion movement from octahedral-to-octahedral sites through a tetrahedral intermediate, providing a more efficient ionic transport route. Consequently, the modification of the crystal framework to incorporate biphasic mixtures enhances the diffusion pathway by transitioning from a 1D to a more favorable 2D structure, which shortens the diffusion length and improves the overall conductivity. While the simulation results indicate a more than twofold increase in conductivity compared to experimental results, this discrepancy is likely due to the nonperiodic features introduced during the ball milling synthesis, including particle size variations and internal strains which are not accounted for in the simulations.

2.3.1. Electrochemical Stability

The performance of $Li_2ZrCl_{6-2x}S_x$ ($0 \leq x \leq 0.5$) SEs was assessed using Li/LPSCl/SE/LPSCl/Li cells through galvanostatic lithium stripping and plating at a current density of 0.1 mA cm^{-2} at 25 °C. Since LZC and LZCS are not directly compatible with metallic Li, LPSCl was incorporated as an interlayer to separate the HSEs from the Li electrodes. Stripping/plating profiles of $Li_2ZrCl_{6-2x}S_x$ ($0 \leq x \leq 0.5$) are depicted in **Figure 7**a. The results clearly indicate that LZCS02 exhibited the lowest polarization. Namely, LZCS02 showed an initial polarization of 38 mV, whereas LZC exhibited a polarization of 74 mV. After 600 h, the polarization of LZC increased significantly to 253 mV, whereas LZCS02 maintained a polarization of 140 mV. The increased initial polarization for LZC is likely attributed to its lower ionic conductivity relative to its sulfur-doped counterparts. The increase in polarization for higher S substitution levels after LZCS03 could likely be attributed to decreased ionic conductivity and interface instability of the electrolyte with LPSCl. In fact, Samanta et al. have already shown that LZC is not entirely stable toward LPSCl due to the higher ion covalency of Zr^{4+} that causes higher reactivity.[36] This could likely explain the increase in polarization over time. To probe this further, the compatibility between LZC/LZCS02 and LPSCl was first examined by monitoring the time-dependent EIS response—over 5 days—of symmetric cells with nonblocking Li metal electrodes. The cell configurations for LZC and LZCS02 were Li/LPSCl/LZC/LPSCl/Li (cell 1) and Li/LPSCl/LZCS02/LPSCl/Li (cell 2), respectively. A control sample with only LPSCl was also measured with the configuration Li/LPSCl/Li (cell 3). The results are presented as a bar diagram in Figure S10a, Supporting Information. The data show that cell 1 exhibits the largest resistance increase over time of ≈65.75 Ω, while cell 2 shows a reduced increase of ≈37.28 Ω. Cell 3 shows the smallest resistance increase of ≈21.23 Ω. This supports the hypothesis that sulfur doping at lower concentrations may suppress the growth of resistive interphases between the two solid electrolytes. Chemical aging tests were also performed in analogous configurations, but with blocking SS electrodes, to avoid interference of lithium metal. The results shown in Figure S10b, Supporting Information evidence a minor chemical aging in the case of LZCS02, with only a 26.83 Ω increase in 5 days. In contrast, LZC, exhibited a sixfold greater increase of 176.02 Ω over the same time. This indicates that by substituting chlorine with sulfur, the interfacial compatibility toward the interlayer (LPSCl) can be improved. To further understand the chemical aging, XPS was measured on chemically aged (a month) LZC/LPSCl and LZCS/LPSCl samples.

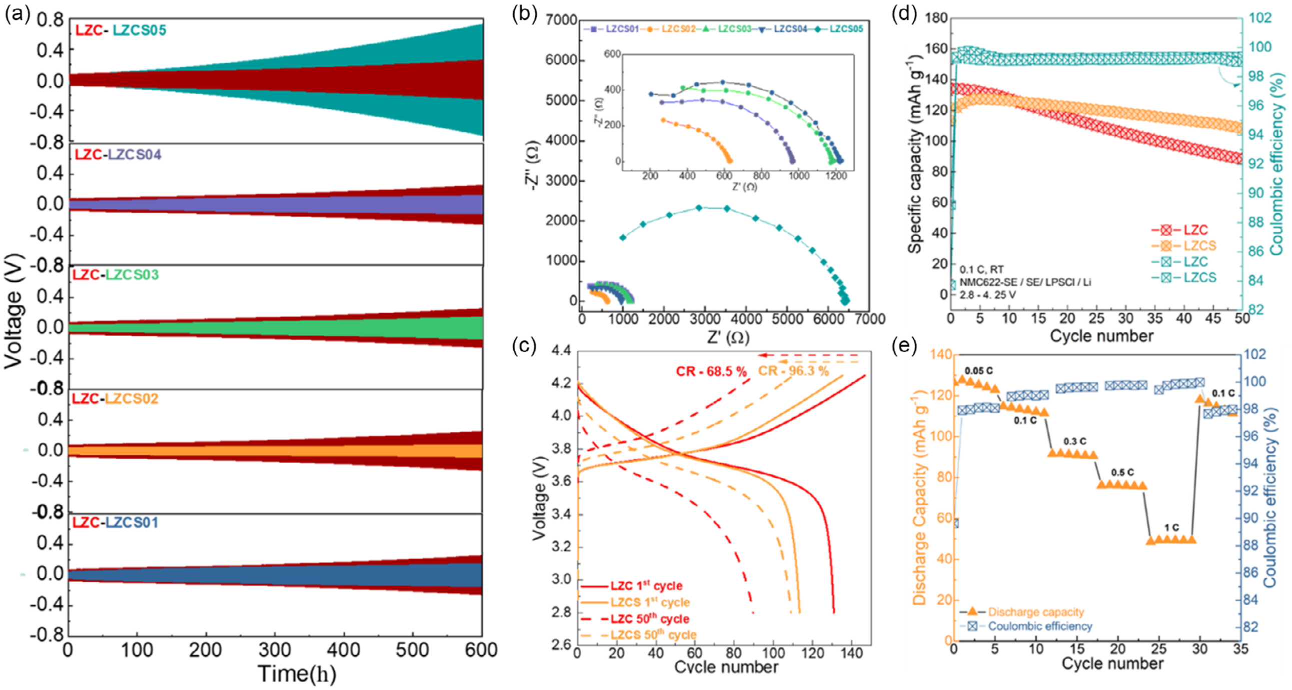

Figure 7. a) Stripping/plating profiles of symmetric cells with $Li_2ZrCl_{6-2x}S_x$ ($0 \leq x \leq 0.5$) SEs and LPSCl interlayer over 600 cycles at a current density of 0.1 mA cm^{-2} with 30 min per stripping/plating step, b) Nyquist plots of LZCS SEs after 600 h of stripping/plating at a current density of 0.1 mA cm^{-2}. The inset shows magnified plots. c) Comparison of the 1st and 50th potential profiles of full cells with LZC and LZCS02 SEs cycled at 0.1 C. The cells were cycled at 25° between 2.8 and 4.25 V. d) Specific discharge capacity of LZC and LZCS02 cells during 50 cycles at 0.1 C. e) Rate compatibility performance of LZCS02 cell at 0.05 C, to 1C, and then 0.1 C again. The SEs are represented by the following colors: LZC (red), LZCS01 (blue), LZCS02 (orange), LZCS03 (green), LZCS04 (violet), and LZCS05 (teal).

The XPS results presented in Figure S11, Supporting Information show no evident chemical changes between the pristine and aged samples for both LZC and LZCS. This suggests that neither system exhibits appreciable chemical degradation when coming in contact with LPSCl. The chemical aging study alone does not provide conclusive evidence regarding the cause of polarization changes. However, we note that expected interfacial products such as Li_2S, LiCl, and Zr–S are difficult to resolve due to overlapping binding energies (Li_2S: 160–162 eV, LiCl: 198–200 eV; Zr–S compounds: 182–185 eV) with the host material. As such, XPS may not be sufficient to resolve subtle interfacial decomposition in these systems. The Nyquist plots provided in Figure 7b further evidence the lower resistance of the symmetric cell with LZCS02 (600 Ω), in comparison to other sulfur-doped variants. Based on these findings, LZCS02 was selected as the optimal candidate for further investigation of full cell performance.

To explore further the electrochemical performance of these electrolytes, a comparative study was conducted on the electrochemical behavior of LZC and LZCS02, using NMC622 as the positive electrode and Li_6PS_5Cl as the separator. Full cells were cycled within the voltage range of 2.8–4.25 V versus Li^+/Li at 0.1 C. Initial Coulombic efficiencies of 83.71 % and 89.21 % were achieved for LZC and LZCS02, respectively, with a specific capacity of 130 and 120 mAh g^{-1}. Notably, no sulfidic oxidative plateau was observed neither in LZC nor in LZCS02, consistent with previous reports.[37] Although sulfur doping improves the bulk ionic conductivity, the interfacial properties and reactivity with the cathode material are also affected. This is supported by the reduced initial Coulombic efficiency (CE = 83.82 %), indicating potential irreversible interfacial reactions or kinetic limitations.[38] However, capacity retention of LZCS after 50 cycles was significantly better, maintaining 96.3% of its initial capacity, compared to only 68.5% for LZC (Figure 7c). Figure 7 d shows the development of specific discharge capacities for both LZC and LZCS02 at 0.1 C for 50 cycles, highlighting the superior electrochemical performance of LZCS02. Additionally, a rate capability test was performed with LZCS02 demonstrating good cyclability and good retention even when cycled back to 0.1 C (Figure 7e). The enhanced ionic conductivity of LZCS02 is likely to contribute to its improved performance, particularly at higher current rates.

FIB line scans were recorded for both the samples after 10 cycles; the corresponding cross-sectional images are shown in **Figure 8**. Figure 8a,b presents the line scans of individual elements when going from the solid electrolyte to the $LiNi_xMn_yCo_{1-x-y}O_2$ (NMC), focusing on the interface between the solid electrolyte and NMC particle. Upon moving from the solid electrolyte to the cathode particle, LZCS exhibits a notable increase in the oxygen signal intensity at the NMC/solid electrolyte contact points, reaching up to 300 counts per second (cps), while LZC shows a significantly higher oxygen signal intensity of around 2000 cps. Similarly, nickel (Ni) diffusion was observed in both samples, with LZCS exhibiting subtle diffusion (<100 cps), while LZC shows a diffusion rate over one order magnitude higher (>1000 cps). Manganese (Mn) and cobalt (Co) diffusion were not detected at the interface. Zr and Cl were present in both samples, with LZC exhibiting <500 cps and LZCS showing values of <250 cps at the interface. These results indicate a lower dissolution of oxygen and transition metals in LZCS, which likely contributes to the improved electrochemical performance of LZCS02 compared to that of LZC, highlighting the beneficial role of S doping in LZC.

The interdiffusion of transition metals in NMC particles, particularly in liquid electrolytes, has been well studied.[39] Recent studies have also explored the impact of transition metal and oxygen dissolution in sulfide-based solid electrolytes with NMC as a positive electrode, which is known to hinder the cycling performance.[40] Recently, Kim et al. demonstrated the electrolyte decomposition of Li_3InCl_6 in contact with the NMC cathodes

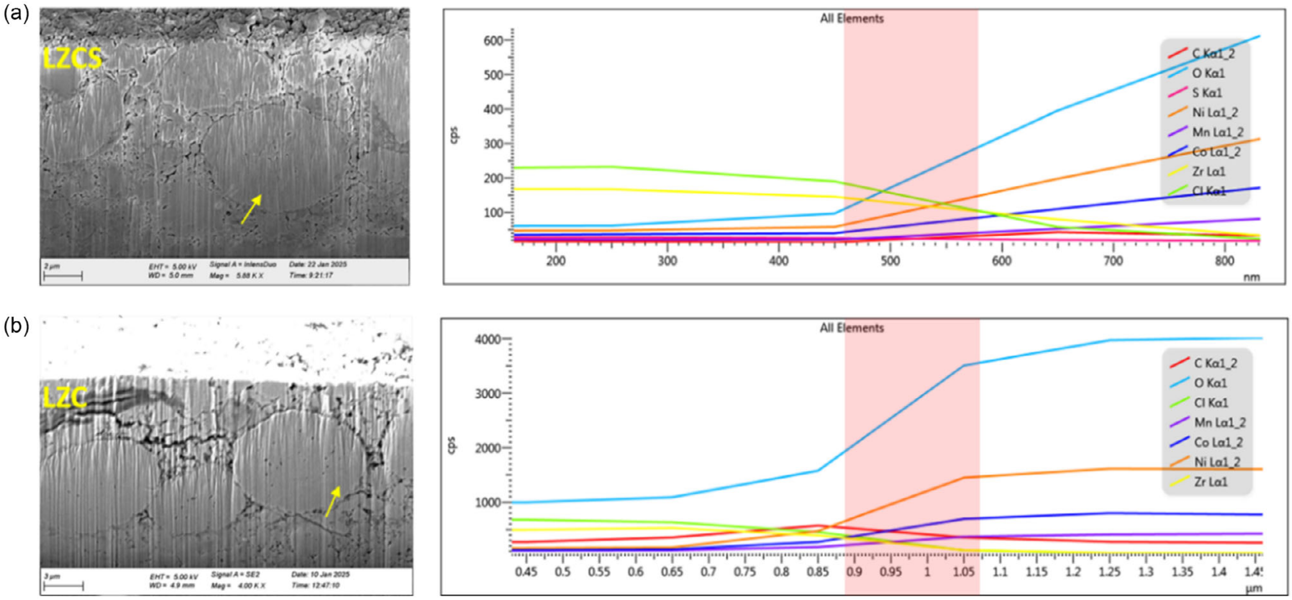

Figure 8. SEM micrographs of FIB-derived cross sections (left) and the respective line scan images (right) of a) LZCS02 and or b) LZC focusing on the NMC/SE/CB composite interfaces after 10 cycles. Yellow arrows indicate the positions of the line scans.

by time-of-flight secondary ion mass spectrometry (TOF–SIMS), revealing the formation of InO_2^- and $LiInO_2^-$ with a simultaneous decrease in NiO^-, MnO^-, and CoO^- fragments.[41] However, to the best of our knowledge, the dissolution of transition metals and oxygen from NMC particles in LZC-based electrolyte has not been previously observed. This study uncovers a critical degradation mechanism in this class of electrolytes. Nonetheless, the FIB line scan provides only a first-hand evidence of transition metal and oxygen diffusion from NMC particles and dissolution in the HESs. Further investigations utilizing advanced characterization techniques, such as transmission electron microscopy (TEM); TOF–SIMS are warranted to provide deeper insights into these processes.

3. Conclusion

In conclusion, we report the development of sulfur-doped biphasic solid-state electrolytes, $Li_2ZrCl_{6-2x}S_x$ ($0 \leq x \leq 0.5$), exhibiting a notable ionic conductivity of 0.64 mS cm^{-1} at 30 °C. The enhanced electrochemical performance of the sulfur-doped electrolytes can be attributed to the increased ionic conductivity, improved polarizability, and the biphasic nature of these materials, as confirmed by EIS and NPD measurements. Theoretical simulations reveal the presence of 2D diffusion pathways in LZCS, which contribute to a reduction in activation energy and promote superior performance. Full cell testing with NMC622 as a positive electrode further highlights the advantage of sulfur doping, with LZCS02 demonstrating a capacity retention of 96.3%, compared to just 68.5% for the undoped LZC. Additionally, FIB–line scans reveal significantly reduced oxygen and nickel interdiffusion in LZCS02 compared to LZC, underscoring the stability benefits of sulfur doping. These findings suggest that fine-tuning the crystal structure by forming biphasic mixtures at certain ratios can open new avenues for enhancing ionic conductivity, thereby offering improved promising routes for the development of high-performance solid electrolytes for practical applications.

4. Experimental Section

Synthesis of $Li_2ZrCl_{6-2x}S_x$

Li_2ZrCl_6 was synthesized by mechanochemical milling using stoichiometric amounts of LiCl (99.9%) and $ZrCl_4$ (99.9%). All raw materials were stored in a glovebox under inert conditions (O_2 and H_2O contents below 1 ppm). For the synthesis, the precursors were placed in an 80 mL jar (yttrium-stabilized zirconia) containing zirconia balls with a diameter of 5 and 10 mm (ball-to-powder weight ratio of 1:20), which was sealed under an argon atmosphere. The precursors were initially mixed at 200 rpm for 2 h to form a homogeneous mixture. After the initial mixing of the powders, high-energy milling (FRITSCH) was performed at 600 rpm for 10 h with 30 min milling followed by a rest period of 30 min to yield Li_2ZrCl_6. For the synthesis of $Li_2ZrCl_{6-2x}S_x$ ($0.1 \leq x \leq 0.5$), a similar procedure as above was followed using stoichiometric amounts of LiCl (99.9%), $ZrCl_4$ (99.9%), and Li_2S (99.9%) all purchased from Sigma Aldrich.

Physicochemical Characterization

Powder X-ray diffraction (XRD) was measured using a STOE STADI-P diffractometer in transmission geometry with a Mo Kα1 source ($\lambda = 0.7093$ Å). The XRD measurements were carried out in the 2θ range from 2 to 50° with a step size of 0.015° (5 h for each sample). Powder samples were sealed inside borosilicate capillaries (diameter 0.5 mm) in the glovebox to avoid any exposure to moisture. Structural studies were performed using Full Prof software, and the resulting crystal structures were visualized using VESTA software.

Neutron diffraction and total scattering were performed on the D2B (high-resolution neutron diffractometer) and D4 (disordered material diffractometer) instruments at Institut Laue-Langevin (ILL, Grenoble, France), respectively.[42,43] The wavelengths used for D2B and D4 were 1.6 and 0.5 Å with germanium (115) and copper (220) monochromators, respectively. Powder samples were loaded and sealed in vanadium (V) cylindrical sample tubes inside an Ar-filled glovebox and then taken out for the measurements at ambient temperature. For the diffraction, NAC ($Na_2Al_2Ca_3F_{14}$) was measured as a standard to account for the instrumental resolution and silicon standard was used for the peak shape function. PDF analysis was carried out based on the total scattering data. An empty holder was measured under the same conditions and used for the background subtraction. PDFgui[44] was used for structure refinement. Fitted parameters were: scale factor, lattice parameters, isotropic atomic displacement parameters, and the particle diameter. Further details on refinement procedure and refinement tables are provided in the supplementary files.

XANES was performed at the ID26 beamline of the European Synchrotron Radiation Facility (ESRF) using the TEXS in-vacuum tender X-ray spectrometer[45] with the HERFD. The storage ring was operated at 6 GeV and 200 mA current. A cryogenically cooled double-crystal monochromator with Si (111) crystals was used to select the incident energy range. HERFD–XANES spectra were measured at the maximum of the S *K*α1 emission lines as a function of incident X-ray energy across the absorption *K*-edge. The absorption spectra were normalized by the integrated area.[46] Energy calibration was applied by aligning the white line of the $CaSO_4$ reference to the one in the ESRF database (2482.5 eV).

SEM together with EDX was performed using a ZEISS Crossbeam 340 microscope. All samples were prepared inside the glove box by placing them on a carbon sticking tape and gently tapping to avoid any loss of powder. After that, they were transferred under inert gas in a transfer shuttle and measured directly. X-ray photoelectron spectroscopy (XPS) measurements were carried out in a Specs XPS system. Sample preparation and transfer were done in a similar way like for SEM. Monochromatic Al Kα radiation (1486.6 eV) was used together with a pass energy of 30 eV at the analyzer (Phoibos 150) for the detailed scans in the S 2p region. The peak fitting was done with CasaXPS using Shirley-type backgrounds and Gaussian–Lorentzian peak shapes (GL30). Furthermore, the expected parameters for the S 2p peak doublet were fixed (peak area ratio 2:1, spin–orbit splitting 1.20 eV).

Electrochemical Characterization

The ionic conductivity and the corresponding activation energy were determined by EIS measurements at various temperatures in the range from 20 to 80 °C using a ModuLab XM potentiostat and force control using a Compredrive lab press. The measurements were collected in a frequency range from 1 MHz to 1 Hz with an amplitude of 10 mV. To prepare the cells for ionic conductivity measurements, a CompreCell 12 was used and 200 mg of solid electrolyte powder was loaded in the 12-mm cell with stainless steel blocking electrodes. All the preparation was performed inside the glove box. The cell was initially subjected to a pressure variation test to obtain the lowest resistance and check for complete densification. From the results obtained, 370 MPa was the lowest pressure at which the electrolyte exhibited the lowest resistance. Hence, 370 MPa was chosen as standard for the densification of solid electrolyte powders before the EIS measurements. For activation energy measurements, EIS was performed from 20 °C to 80 °C in steps of 10 °C with a rest period between each temperature of 1 h. The electronic conductivities of HSEs were measured with the solid-state cells by DC (direct current) at 0.1 V using stainless steel as blocking electrodes for 12 h.

Li stripping/plating performance measurements were carried out in the cell configuration Li| Li_6PS_5Cl|LZCS| Li_6PS_5Cl|Li at a current density of 0.1 mA cm^{-2} with an alternating 30 min stripping and 30 min plating in a home-made solid-state cell with a diameter of 13 mm. LPSCl was added to prevent the side reaction between the electrolyte and Li. 50 mg of LPSCl was first pressed at 100 MPa for 1 min followed by subsequent addition of 100 mg of LZCS pressed at 100 MPa for 1 min. Another layer of LPSCl (50 mg) on top of LZCS was added, and the trilayer was pressed together at 225 MPa and then attached to 50 μm lithium foils on both sides. A torque of 3 N m^{-1} was applied to close the cell and to hold the pressure. The cells were sealed in pouch bags to avoid exposure to moisture and cycled at 25 ° C. The performance of LZC and LZCS as the electrolyte materials was tested in full cells using $LiNi_{0.6}Mn_{0.2}Co_{0.2}O_2$ (NMC622) as a positive electrode. For the battery assembly, NMC622/HSE/Carbon black (CB)|HSE|Li_6PS_5Cl|Li configuration was used with an NMC: HSE: CB (composite mixture) weight ratio of 70:27.5:2.5 at the positive electrode. The composite mixture was manually ground for 30 min and used without further mixing. Lithium was initially attached to the current collector followed by the addition of 100 mg of LPSCl, which was then pressed at 100 MPa. Subsequently, 100 mg of LZC or LZCS02 was added and pressed at 100 MPa. The cathode mixture was prepared with a mass loading of 5−6 mg cm^{-2} of active material (NMC) and pressed at 370 MPa for 3 min. A torque of 3 N m^{-1} was applied to seal the cells, which were then cycled at 0.1 C at 25 ° C in a climatic chamber. The same procedure was employed for cells used in rate capability tests.

Computational Details

Density functional theory (DFT) calculations were performed using the generalized gradient approximation (GGA) and the Perdew–Burke–Ernzerhof (PBE) exchange–correlation functional[47] within the framework of the projected augmented wave (PAW) approach,[48,49] as implemented in the Vienna ab initio simulation package (VASP). Dispersion interactions were modeled using Grimme's third-generation (D3) semi-empirical van der Waals corrections[50] during structural optimization.

The calculations utilized a plane-wave basis set with a cutoff energy of 520 eV, and the Brillouin zone was sampled using a $2 \times 2 \times 4$ k-point grid within the Monkhorst–Pack scheme.[51] The electronic energy convergence criterion was set to 10^{-5} eV, ensuring high accuracy in energy minimization.

The initial nonmagnetic moments were set according to the expected magnetic behavior of the system. Structural optimization was conducted by relaxing both the atomic positions and the lattice parameters until the forces acting on all atoms were below 0.01 eV$Å^{-1}$. The initial atomic configurations were constructed based on experimental crystallographic data. To introduce sulfur (S) doping into the system while maintaining stoichiometry, two chlorine (Cl) atoms were removed and replaced with S atoms at distinct positions within the lattice. These substitutions were strategically performed in two configurations: one where the Cl atoms were spatially close to each other and another where they were far apart. This approach allowed us to investigate the effects of dopant distribution on the electronic and structural properties of the system.

To study the diffusion pathway, bond-valence site energy (BVSE) calculations[52,53] were performed using a two-body Morse-type force field based on the bond-valence approach, employing geometry-optimized structural models derived from the above-described DFT calculations. The BVSE approach is widely recognized as an efficient and reliable method for predicting ion migration pathways and roughly estimating energy barriers based on local structural information. In this framework, the BVSE approach is utilized to predict the optimal Li^+ migration pathways, which are represented by regions of low BVSE energy. To better illustrate the ion migration, these regions can be visualized using a 3D representation, where surfaces outline the accessible low-BVSE regions for the charge carrier.[54,55] A continuous conduction path was established when these regions span the entire structure. To identify such pathways, the isosurface value can be gradually increased until a fully connected structure emerges. The activation barriers for carrier hopping were then determined by the climbing image nudged elastic band (cNEB) method.[56,57] The diffusion path was first constructed by the linear interpolation of atomic coordinates between initial and final states with four distinct images, followed by relaxation until the forces on all atoms were below 0.01 eV $Å^{-1}$. Large supercells were used to ensure ion isolation from periodic images (ions separated by at least 10 Å).

Acknowledgements

This work contributes to the research performed at CELEST (Center for Electrochemical Energy Storage Ulm-Karlsruhe) and was partly funded by the German Research Foundation (DFG) under Project ID 390874152 (POLiS Cluster of Excellence). The authors acknowledge ESRF (Grenoble, France) for the provision of experimental facilities. The authors thank the ILL for the provision of beamtime at D2B and D4 beamlines under the proposal 6-06-536 (data: doi:10.5291/ILL-DATA.6-06-536). *The authors are also grateful for the utilization of ID26 beamline at ESRF under the proposal CH6862 (Data: doi.org/10.15151/ESRF-ES-1435811659)* and would like to thank Dr. Blanka Delefts for assistance. J.L. and A.V. would like to acknowledge financial support from the Federal Ministry for Economic Affairs and Climate Action (BMWK) and the Federal Ministry of Education and Research (BMBF) in the frame of the REFA (03EI6055B) and ELIC (03ETE034C) projects, as well as the Helmholtz Association. This project received funding from the European Union's Horizon 2020 research and innovation program under grant agreement no. 957189. Computer time provided by the state of Baden-Württemberg through bwHPC and the German Research Foundation (DFG) through grant no INST 40/575-1 FUGG (JUSTUS 2 cluster) is gratefully acknowledged.

Open Access funding enabled and organized by Projekt DEAL.

Conflict of Interest

The authors declare no conflict of interest.

Author Contributions

Priya Ganesan designed and carried out the structural and electrochemical experiments, NPD, and NPDF, analyzed, discussed the data, and wrote the manuscript. **Jianneng Liang** supervised and discussed the data. **Ramon Zimmermanns** carried out NPDF analysis, refinement, and discussed the data. **Gabriel J. Cuello** and **Inés Puente Orench** carried out neutron diffraction experiments and helped with the analysis. **Thomas Diemant** performed the XPS experiments. **Yang Hu** performed XANES, NPD, and NPDF measurements. **Sebastian Baumgart** and **Mohsen Sotoudeh** carried out the computational simulations under the supervision of **Axel Groß**, **Maximilian Fichtner** supervised the work, discussed the data, and provided funding. **Alberto Varzi** supervised, and discussed the data. All authors reviewed the final version of the manuscript.

Data Availability Statement

The data that support the findings of this study are available from the corresponding author upon reasonable request.

Keywords: full cells · Li_2ZrCl_6 · NMC · solid electrolytes · unit cell volumes

[1] J. B. Goodenough, Y. Kim, *Chem. Mater.* **2010**, *22*, 587.
[2] J. Janek, W. G. Zeier, *Nat. Res.* **2023**, *8*, 230.
[3] Y. Ren, T. Danner, A. Moy, M. Finsterbusch, T. Hamann, J. Dippell, T. Fuchs, M. Müller, R. Hoft, A. Weber, L. A. Curtiss, P. Zapol, M. Klenk, A. T. Ngo, P. Barai, B. C. Wood, R. Shi, L. F. Wan, T. W. Heo, M. Engels, J. Nanda, F. H. Richter, A. Latz, V. Srinivasan, J. Janek, J. Sakamoto, E. D. Wachsman, D. Fattakhova-Rohlfing, *Adv. Energy Mater.* **2023**, *13*, 220193.
[4] S. Yang, Y. Tang, Y. Yao, S. He, Z. Wu, Y. Yang, H. Pan, X. Rui, Y. Yu, *Mater. Horiz.* **2025**, *12*, 1058.
[5] S. Zeng, K. Ren, H. Ding, S. Xu, H. W. Li, Y. Li, *Chem. Commun.* **2025**, *61*, 929.
[6] X. Nie, J. Hu, C. Li, *Interdiscip. Mater.* **2023**, *2*, 365.
[7] H. Ito, K. Shitara, Y. Wang, K. Fujii, M. Yashima, Y. Goto, C. Moriyoshi, N. C. Rosero-Navarro, A. Miura, K. Tadanaga, *Adv. Sci.* **2021**, *8*, 2101413.
[8] Z. Liu, P. H. Chien, S. Wang, S. Song, M. Lu, S. Chen, S. Xia, J. Liu, Y. Mo, H. Chen, *Nat. Chem.* **2024**, *16*, 1584.
[9] K. Kim, D. Park, H. G. Jung, K. Y. Chung, J. H. Shim, B. C. Wood, S. Yu, *Chem. Mater.* **2021**, *33*, 3669.
[10] S. R. Combs, P. K. Todd, P. Gorai, A. E. Maughan, *J. Electrochem. Soc.* **2022**, *169*, 040551.
[11] Y. Liu, S. Wang, A. M. Nolan, C. Ling, Y. Mo, *Adv. Energy Mater.* **2020**, *10*, 2002356.
[12] S. Wang, Q. Bai, A. M. Nolan, Y. Liu, S. Gong, Q. Sun, Y. Mo, *Angew. Chem.* **2019**, *131*, 8123.
[13] B. Tao, D. Zhong, H. Li, G. Wang, H. Chang, *Chem. Sci.* **2023**, *14*, 8693.
[14] K. Wang, Q. Ren, Z. Gu, C. Duan, J. Wang, F. Zhu, Y. Fu, J. Hao, J. Zhu, L. He, C. W. Wang, Y. Lu, J. Ma, C. Ma, *Nat. Commun* **2021**, *12*, 4410.
[15] T. Asano, A. Sakai, S. Ouchi, M. Sakaida, A. Miyazaki, S. Hasegawa, *Adv. Mater.* **2018**, *30*, 1803075.
[16] R. Xiong, L. Yuan, R. Song, S. Hao, H. Ji, Z. Cheng, Y. Zhang, B. Jiang, Y. Shao, Z. Li, Y. Huang, *ACS Appl. Mater. Interfaces* **2024**, *16*, 36281.
[17] E. Sebti, H. A. Evans, H. Chen, P. M. Richardson, K. M. White, R. Giovine, K. P. Koirala, Y. Xu, E. Gonzalez-Correa, C. Wang, C. M. Brown, A. K. Cheetham, P. Canepa, R. J. Clément, *J. Am. Chem. Soc.* **2022**, *144*, 5795.
[18] R. Schlem, S. Muy, N. Prinz, A. Banik, Y. Shao-Horn, M. Zobel, W. G. Zeier, *Adv. Energy Mater.* **2020**, *10*, 1903719.
[19] K. Tuo, C. Sun, S. Liu, *Electrochem. Energy* **2023**, *6*, 17.
[20] S. Chen, C. Yu, S. Chen, L. Peng, C. Liao, C. Wei, Z. Wu, S. Cheng, J. Xie, *Chin. Chem. Lett.* **2022**, *33*, 4635.
[21] Q. Shao, C. Yan, M. Gao, W. Du, J. Chen, Y. Yang, J. Gan, Z. Wu, W. Sun, Y. Jiang, Y. Liu, M. Gao, H. Pan, *ACS Appl. Mater. Interfaces* **2022**, *14*, 8095.
[22] S. P. Culver, A. G. Squires, N. Minafra, C. W. F. Armstrong, T. Krauskopf, F. Böcher, C. Li, B. J. Morgan, W. G. Zeier, *J Am Chem Soc.* **2020**, *142*, 21210.
[23] K. Tuo, F. Yin, F. Mi, C. Sun, *J. Energy Chem.* **2023**, *87*, 12.
[24] Z. Song, T. Wang, H. Yang, W. H. Kan, Y. Chen, Q. Yu, L. Wang, Y. Zhang, Y. Dai, H. Chen, W. Yin, T. Honda, M. Avdeev, H. Xu, J. Ma, Y. Huang, W. Luo, *Nat. Commun* **2024**, *15*, 1481.
[25] X. Li, J. T. Kim, J. Luo, C. Zhao, Y. Xu, T. Mei, R. Li, J. Liang, X. Sun, *Nat. Commun* **2024**, *15*, 53.
[26] T. Dai, S. Wu, Y. Lu, Y. Yang, Y. Liu, C. Chang, X. Rong, R. Xiao, J. Zhao, Y. Liu, W. Wang, L. Chen, Y. S. Hu, *Nat. Energy* **2023**, *8*, 1221.
[27] S. Kmiec, E. Ruoff, A. Manthiram, *Angew. Chem., Int. Ed.* **2025**, *64*, e202416979.
[28] E. van der Maas, W. Zhao, Z. Cheng, T. Famprikis, M. Thijs, S. R. Parnell, S. Ganapathy, M. Wagemaker, *J. Phys. Chem. C* **2023**, *127*, 125.
[29] P. Ganesan, M. Soans, M. A. Cambaz, R. Zimmermanns, R. Gond, S. Fuchs, Y. Hu, S. Baumgart, M. Sotoudeh, D. Stepien, H. Stein, A. Groß, D. Bresser, A. Varzi, M. Fichtner, *ACS Appl. Mater. Interfaces* **2023**, *15*, 38391.
[30] D. Xu, J. He, Y. He, S. Wang, G. Wu, M. Li, H. Cheng, K. Yu, X. Huang, B. Tian, *J. Mater. Chem. A* **2024**, *12*, 27694.
[31] J. Cheng, H. Zhang, Z. Wang, Y. Zhou, K. Yu, Y. Cheng, Z. Yu, X. Huang, B. Tian, *J. Energy Storage* **2024**, *89*, 111700.
[32] H. Kwak, D. Han, J. P. Son, J. S. Kim, J. Park, K. W. Nam, H. Kim, Y. S. Jung, *Chem. Eng. J.* **2022**, *437*, 135413.
[33] L. Zhang, D. Sun, J. Kang, H. T. Wang, S. H. Hsieh, W. F. Pong, H. A. Bechtel, J. Feng, L. W. Wang, E. J. Cairns, J. Guo, *Nano Lett.* **2018**, *18*, 4506.
[34] W. G. Zeier, R. Schlem, A. Banik, M. Eckardt, M. Zobel, *ACS Appl. Energy Mater.* **2020**, *3*, 10164.
[35] M. Sotoudeh, S. Baumgart, M. Dillenz, J. Döhn, K. Forster-Tonigold, K. Helmbrecht, D. Stottmeister, A. Groß, *Adv. Energy Mater.* **2024**, *14*, 2302550.
[36] S. Samanta, S. Bera, R. K. Biswas, S. Mondal, L. Mandal, A. Banerjee, *ACS Energy Lett.* **2024**, *9*, 3683.
[37] S. Y. Kim, K. Kaup, K. H. Park, A. Assoud, L. Zhou, J. Liu, X. Wu, L. F. Nazar, *ACS Mater. Lett.* **2021**, *3*, 930.
[38] E. Kaeli, Z. Jiang, X. Yang, E. P. K. L. Choy, N. B. Liang, E. Barks, S. Wang, S. D. Kang, W. C. Chueh, *Energy, Environ. Sci.* **2025**, *18*, 1452.
[39] Z. Ruff, C. Xu, C. P. Grey, *J. Electrochem Soc.* **2021**, *168*, 060518.
[40] R. Zhang, F. Strauss, L. Jiang, L. Casalena, L. Li, J. Janek, A. Kondrakov, T. Brezesinski, *Chem. Commun.* **2023**, *59*, 4600.
[41] W. Kim, J. Noh, S. Lee, K. Yoon, S. Han, S. Yu, K. H. Ko, K. Kang, *Adv. Mater.* **2023**, *35*,2301631
[42] H. E. Fischer, G. J. Cuello, P. Palleau, D. Feltin, A. C. Barnes, Y. S. Badyal, J. M. Simonson, *Appl. Phys. A: Mater. Sci. Process.* **2002**, *74*, s160.
[43] A. W. Hewat, *Mater. Sci. Forum* **1986**, *9*, 69.
[44] C. L. Farrow, P. Juhas, J. W. Liu, D. Bryndin, E. S. Boin, J. Bloch, T. Proffen, S. J. L. Billinge, *J. Phys.:Condens. Matter* **2007**, *19*, 335219.
[45] P. Glatzel, A. Harris, P. Marion, M. Sikora, T. C. Weng, C. Guilloud, S. Lafuerza, M. ovezzi, B. Detlefs, L. Ducotté, *J. Synchrotron Radiat.* **2021**, *28*, 362.
[46] L. Bugarin, H. A. Suarez Orduz, P. Glatzel, *J. Synchrotron Radiat.* **2024**, *31*, 1118.
[47] J. P. Perdew, K. Burke, M. Ernzerhof, *Phys. Rev. Lett.* **1996**, *77*, 3865.
[48] P. E. Blochl, Projector augmented-+rave method, Vol. 50.
[49] G. Kresse, D. Joubert, *Phys. Rev. B.*, *59*, 1758.
[50] S. Grimme, J. Antony, S. Ehrlich, H. Krieg, *J. Chem. Phys.* **2010**, *132*, 154104.
[51] H. J. Monkhorst, J. D. Pack, *Phys. Rev. B.* **1976**, *13*, 5188.
[52] I. D. Brown, *Chem. Rev.* **2009**, *109*, 6858.
[53] S. Adams, J. Swenson, PACS numbers: 66.30.Hs, 61.43.Fs, 66, Vol. 30, Dn **2000**.
[54] J. Cabana, C. D. Ling, J. Oró-Solé, D. Gautier, G. Tobías, S. Adams, E. Canadell, M. R. Palacín, *Inorg. Chem.* **2004**, *43*, 7050.
[55] S. Adams, J. Swenson, *Phys. Rev. B: Condens. Matter Mater. Phys.* **2001**, *63*, 542011.
[56] G. Henkelman, B. P. Uberuaga, H. Jónsson, *J. Chem. Phys.* **2000**, *113*, 9901.
[57] G. Henkelman, H. Jónsson, *J. Chem. Phys.* **2000**, *113*, 9978.

Manuscript received: May 20, 2025
Revised manuscript received: June 6, 2025
Version of record online: July 3, 2025